Electronic supplement for

Spatially heterogenous Holocene slip rates drive seismic sequence variability on a normal fault

Constanza Rodriguez Piceda^{1*}, Zoë K. Mildon¹, Billy J. Andrews¹, Francesco Visini², Jean-Paul Ampuero³, Martijn van den Ende³

¹ University of Plymouth, School of Geography, Earth and Environmental Sciences, Plymouth, United Kingdom

² National Institute of Geophysics and Volcanology (INGV), Italy

³ Université Côte d'Azur, Observatoire de la Côte d'Azur, IRD, CNRS, Géoazur, Nice, France

*Corresponding email: constanza.rodriguezpiceda@plymouth.ac.uk

Contents of this file

Text S1: determination of mesh resolution

Text S2: determination of depth-distribution of normal stress

Text S3: seismic hazard calculations

Table S1: Model set-up describing material and frictional properties, fault geometry and resolution

Table S2: Field-based values of slip rate

Table S3: a/b ratios of models for sensitivity analysis of rate-and-state friction parameters

Figure S1: schematic diagram of distances relevant to seismic hazard calculations

<u>Figure S2</u>: Slip rate evolution for models "all data spline", "boxcar mean", "boxcar min", "triangular mean", "triangular nin", "triangular right", "elliptical mean" and "elliptical min".

<u>Figure S2-S7:</u> Magnitude-frequency and recurrence distributions of earthquake sequences for models with alternative a/b ratios.

<u>Figure S8:</u> Magnitude-frequency and recurrence distributions of earthquake sequences for models with downdip variations of long-term slip rate.

<u>Figure S9</u>: seismic hazard curves for models "all data spline", "boxcar mean", "boxcar min", "triangular mean", "triangular nin", "triangular right", "elliptical mean" and "elliptical min" for sites Avezzano and Sulmona

Text S1. Rate-and-state friction governing equations

QDYN implements adaptive time-stepping to balance the computation time between the coseismic and interseismic periods. Friction evolution on the fault follows the classical form of rate-and-state which considers that the fault is always slipping with the shear stress (τ) equal to the fault strength (Dieterich, 1979; Ruina, 1983; Marone, 1998):

$$\tau = \mu \sigma$$
 (S1)

where σ is the effective normal stress and μ the friction coefficient. The latter depends on the slip rate (V) and a state variable (θ)

$$\mu(\theta, V) = \mu_0 + a \ln\left(\frac{V}{V_0}\right) + b \ln\left(\frac{V_0 \theta}{D_c}\right) \quad (S2)$$

where μ_0 is the reference coefficient of friction at reference slip rate V_0 and D_c the characteristic distance over which the evolution towards a new steady state takes place. The material parameters a and b quantify the contribution of slip rate V and of state θ to the friction, respectively. Velocity-strengthening materials are characterized by a>b. Velocity weakening materials display a
b and are conditionally stable: they produce stable sliding if they occupy a fault length smaller than a so-called limiting value of the nucleation length (L_∞) and stickslip behavior otherwise (Eq. 4, Rubin and Ampuero, 2005):

$$L_{\infty} = \frac{1}{\pi} \left(\frac{b}{b-a} \right)^2 \frac{GD_c}{b\sigma}$$
 (S3)

where G is the shear modulus.

The state θ evolution is described by the ageing law (Dieterich, 1979; Ruina, 1983):

$$\frac{d\theta}{dt} = 1 - \frac{V\theta}{D_c} \quad (S4)$$

The minimum length scale that needs to be resolved by the numerical grid is the process, or cohesive, zone length (L_b):

$$L_b = \frac{GD_c}{h\sigma} \tag{S5}$$

Lb must be at least three time larger than the element size. Accordingly, we set $L_b/\Delta x \sim 9$ and $L_b/\Delta w \sim 5$.

The emergence of full and partial ruptures on a fault is controlled by the ratio of its shortest length (W) to the nucleation length L_{∞} (Rubin & Ampuero, 2005; Eq. 4). Seismic events emerge when W > L_{∞} . Complex slip patterns, involving full and partial ruptures, can emerge if W is sufficiently large (Barbot, 2019; Cattania, 2019; Cattania and Segall, 2019; Heimisson, 2020). Studies have shown that the minimum W/ L_{∞} ratio where this occurs depends on the model dimensionality and asperity shape. 1D faults generate complex seismic sequences with W/ L_{∞} > 10 (Cattania, 2019), whereas in 2D fault planes with circular asperities partial ruptures are able to occur with W/ L_{∞} = 10.2 (Cattania and Segall, 2019). Therefore, by setting W/ L_{∞} = 20.7 we ensure that, under spatially homogenous loading rate conditions, the fault generates only full ruptures, so we can isolate the effect of the variable slip rates driving the complexity of the seismic sequence (for details of frictional parameters, fault geometry and resolution, see Table S1).

Table S1: Model set-up describing material and frictional properties, fault geometry and resolution. VW= velocity weakening region, VS= velocity-strengthening region; *following Lapusta et al. (2000) and accounting for the dip angle (60.4°, see Text S2).

Symbol	Description (units)	Value		
Material properties				
G	Shear modulus (Pa)	3e10		
λ	Elastic modulus (Pa)	3e10		
С	Shear wave velocity (m/s)	3000		
Frictional pro	perties			
µ*	Reference friction coefficient	0.6		
а	Direct-effect parameter	0.007		
b	Evolution effect parameter	0.014 (VW) / 0.0042 (VS)		
Dc	Characteristic slip distance (m)	10e-3		
σ	Initial effective normal stress (Pa)	43.5e6*		
Lb	Process zone width (m)	492.6		
	<u>G. Dc</u>			
	$b.\sigma$			
L∞	Limiting nucleation length value (m)	627.2		
	$\frac{1}{\pi} \left(\frac{b}{b-a} \right)^2 L_b$			
Geometry				
Lf	Fault segment length (km)	7		

Wf	Fault segment width (km)	17
L	Velocity-weakening length (km)	6.4
W	Velocity-weakening width (km)	13
Δχ	Along-strike element size (m)	54.7
Δw	Along-dip element size (m)	98.8
N	Number of individual fault elements	22016
Nx	Number of fault elements along strike	128
Nw	Number of fault elements across strike	172
Ratio $L_b/\Delta x$ $(L_b/\Delta w)$	Ratio for mesh resolution	9 (5)
Z_corner	Depth of fault bottom (km b.m.s.l.)	-15

Text S2: Dip correction for normal stress

Lapusta et al. (2000) proposes that the variation of effective normal stress with depth for a strike-slip fault is as following: effective normal stress is equal to the lithostatic pressure minus the hydrostatic pore pressure at shallow depth (up to 2.6 km), with a transition to lithostatatic pore pressure gradient with a 50 MPa offset at depth (z):

$$\bar{\sigma}_l = min \begin{cases} 50 MPa \\ 2.8 + 18 z/km \end{cases} (S6)$$

We account for the dip angle of the normal fault (α) in our simulation:

$$\bar{\sigma} = \bar{\sigma}_l * \sin(\alpha)$$
 (S7)

Table S2: values of preferred slip rate (ordered from NW to SE) calculated from field-throw rate measurements with corresponding references (Faure Walker *et al.*, 2019).

# Throw	Preferred value	Minimum	Maximum value	Reference	Distance
measurement	of slip rate	value of	of slip rate		along
	(mm/yr)	slip rate	(mm/yr)		rectified
		(mm/yr)			trace (km)
1	0.48	0.3	0.78	(Roberts and	0.55
				Michetti, 2004)	
2	0.25	0.16	0.4	(Faure Walker	1.87
				et al., 2009)	
3	0.75	0.48	1.18	(Faure Walker	3.18
				et al., 2009)	

4	0.64	0.4	1.02	(Roberts and	3.62
				Michetti, 2004)	
5	0.63	0.4	1	(Faure Walker	3.89
				et al., 2012)	
6	0.62	0.39	0.99	(Cowie et al.,	3.89
				2017)	
7	0.41	0.26	0.55	(Papanikolaou	4.45
				et al., 2005)	

Table S3: Variations of rate-and-state friction parameters a and b to perform sensitivity analysis

a	b	a/b	a-b
0.007	0.016	0.44	-0.009
0.001	0.004	0.25	-0.003
0.001	0.006	0.17	-0.005
0.001	0.008	0.13	-0.007
0.001	0.01	0.1	-0.009

Text S3: Seismic hazard calculations

We used the ground motion prediction equations (GMPEs) calibrated to the Italy region by Bindi et al. (2011). These GMPEs solve for the geometric mean of the horizontal and vertical components of peak ground acceleration (PGA) generated by an event of magnitude M at a site with a specified Joyner-Boore distance (R_{jb}, defined as the shortest distance from the site to the surface projection of the fault) (Fig. S1).

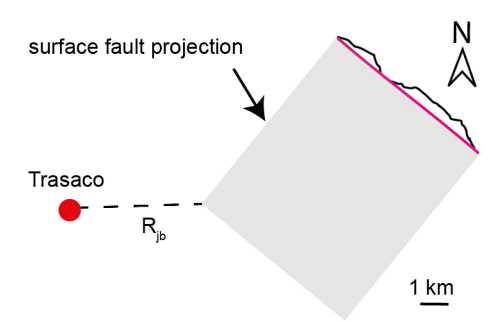


Figure S1: schematic diagram showing field-based (black) and rectified (magenta) fault surface trace, horizontal projection of fault surface (grey) and the Joyner-Boore distance (R_{jb}, dashed black line) to the chosen site (red marker) used for the hazard estimations.

The probability of exceedance (PoE) for a single event at a given intensity measure level –in this case, horizontal PGA- is derived from the complement of the cumulative distribution function (CDF):

$$PoE_{event}(IML) = 1 - F_{event}(log_{10}IML)$$
 (S8)

where Fevent is the CDF of the log-normal distribution for the event ground motion model:

$$F_{event}(log_{10}IML) = \phi\left(\frac{log_{10}IML - \mu_{event}}{\sigma}\right)$$
 (S9)

where ϕ is the standard normal CDF, μ_{event} the mean ground motion $log_{10}Y$ predicted for the event and σ the standard deviation of the logarithmic ground motion.

The annual probability of exceedance for an event is the product of the event-level PoE and the annual rate of occurrence of the event λ_{event} :

Annual
$$PoE_{event}(IML) = Annual PoE_{event}(IML) \lambda_{event}$$
 (S10)

Where λ_{event} is calculated as the inverse of the catalog length $T_{catalog}$ (i.e. duration of the seismic catalog for the current model in years):

$$\lambda_{event} = \frac{1}{T_{catalog}}$$
 (S11)

The total PoE for a model is computed using the complement product approach across the total n events in the simulation

$$PoE_{model}(IML) = 1 - \sum_{n} (1 - PoE_{event}(IML))$$
 (S12)

Equivalently, the annual PoE for a model at a given IML $PoE_{model}(IML)$ is aggregated using the complement product approach for the annual PoE of individual events:

Annual
$$PoE_{model}(IML) = 1 - \sum_{n} (1 - Annual PoE_{event}(IML))$$
 (S13)

This workflow has been implemented step-by-step into a Jupyter Notebook. A step-by-step workflow of the computation of hazard curves from the synthetic seismic catalogs can be found in (Rodriguez Piceda, 2025)

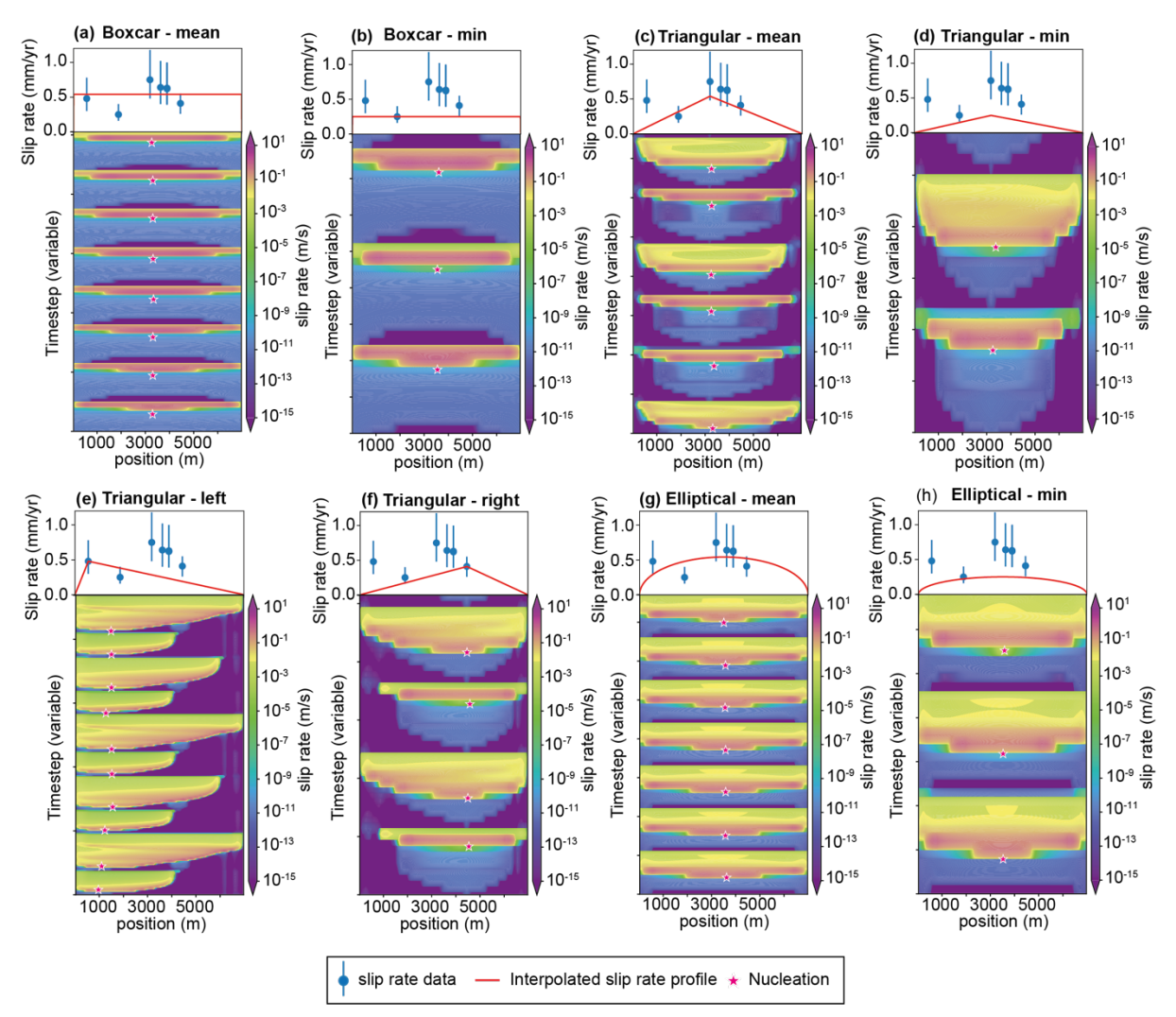


Figure S2: Top subpanels: Long-term slip rate profiles along the fault for each of the models based on 7 estimations derived from field throw measurements along the Parasano-Pescina fault shown as blue markers (Faure Walker et al., 2021 and references therein). In all the models the long-term slip rate it tapered to 0.001 mm/yr at the borders. Bottom subpanels: Evolution of the slip rate along a horizontal profile taken at the middle of the fault between 20,000 and 40,000 years for loading-rate profiles: (a) "triangular max" uses the maximum value of slip rate (measurement #3); (b) "left triangular" uses measurement #1 with a linear interpolation, (c) "right triangular" uses measurement #7 with a linear interpolation; (d) "triangular mean" uses the mean slip rate value centered in middle of the fault with a linear interpolation; (e) "triangular min" uses the minimum slip rate value (measurement #2) centered in middle of the fault with a linear interpolation;); (f) "box car mean" uses only the average value of slip rate; (f) "box car min" uses only the minimum value of slip rate (measurement #2); ; (g) semiellipse mean" uses the mean value of slip rate (measurement #2) with a semielliptical interpolation; (h) "semiellipse min" uses the min value of slip rate (measurement #2) with a semielliptical interpolation. Magenta stars show the nucleation location. Note that, due to QDYN's adaptive time-stepping, in the co-seismic period timesteps are smaller than in the inter-seismic period.

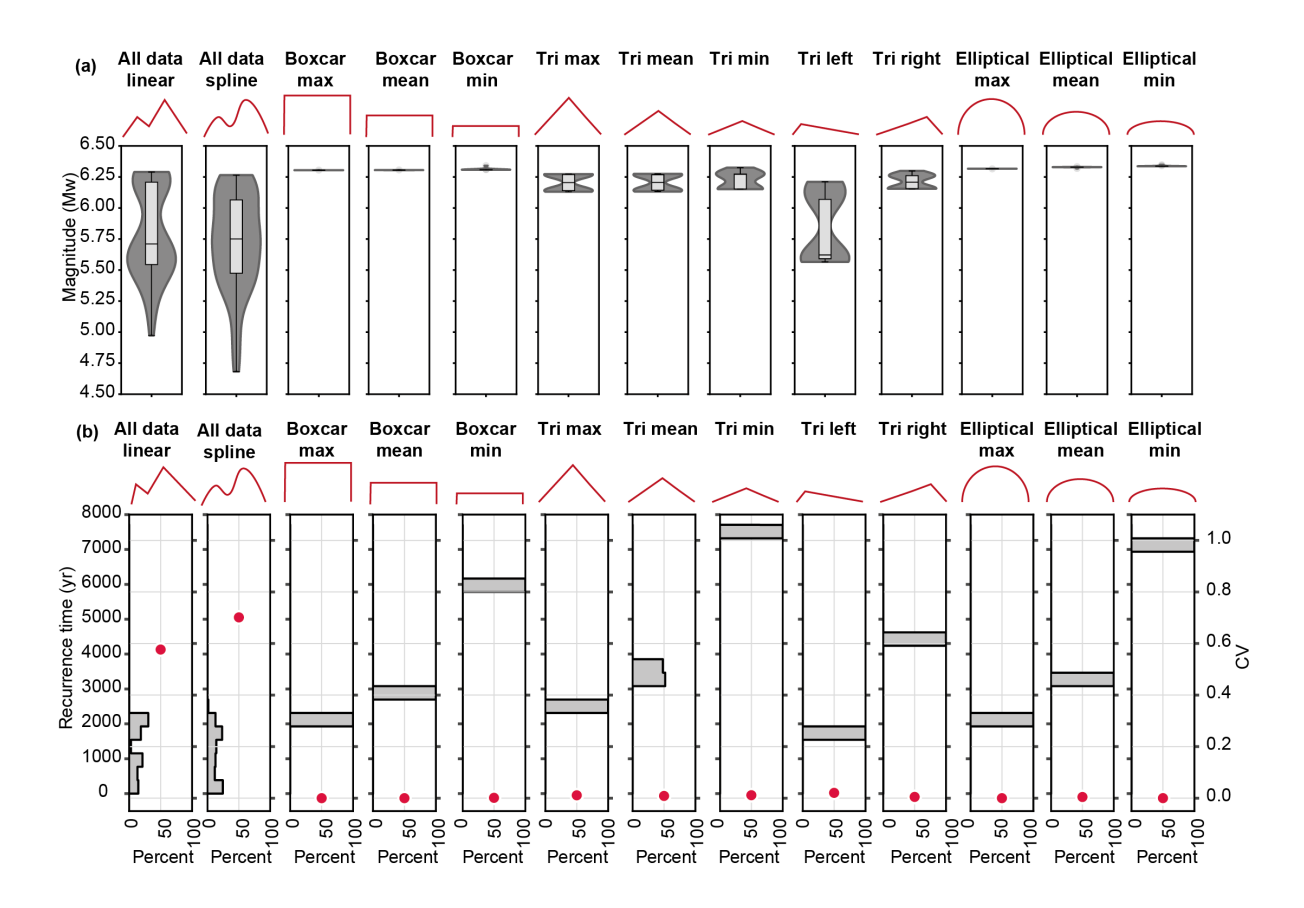


Figure S3: (a) Magnitude-frequency distribution shown as kernel-density functions for model with a=0.007 and b=0.016 (a/b=0.44); **(b)** Coefficient of variation (CV, red dots) and histogram of recurrence time (T_r, grey bars) for each simulation. For descriptions of the slip rate profiles, see Fig. 3 in the main text.

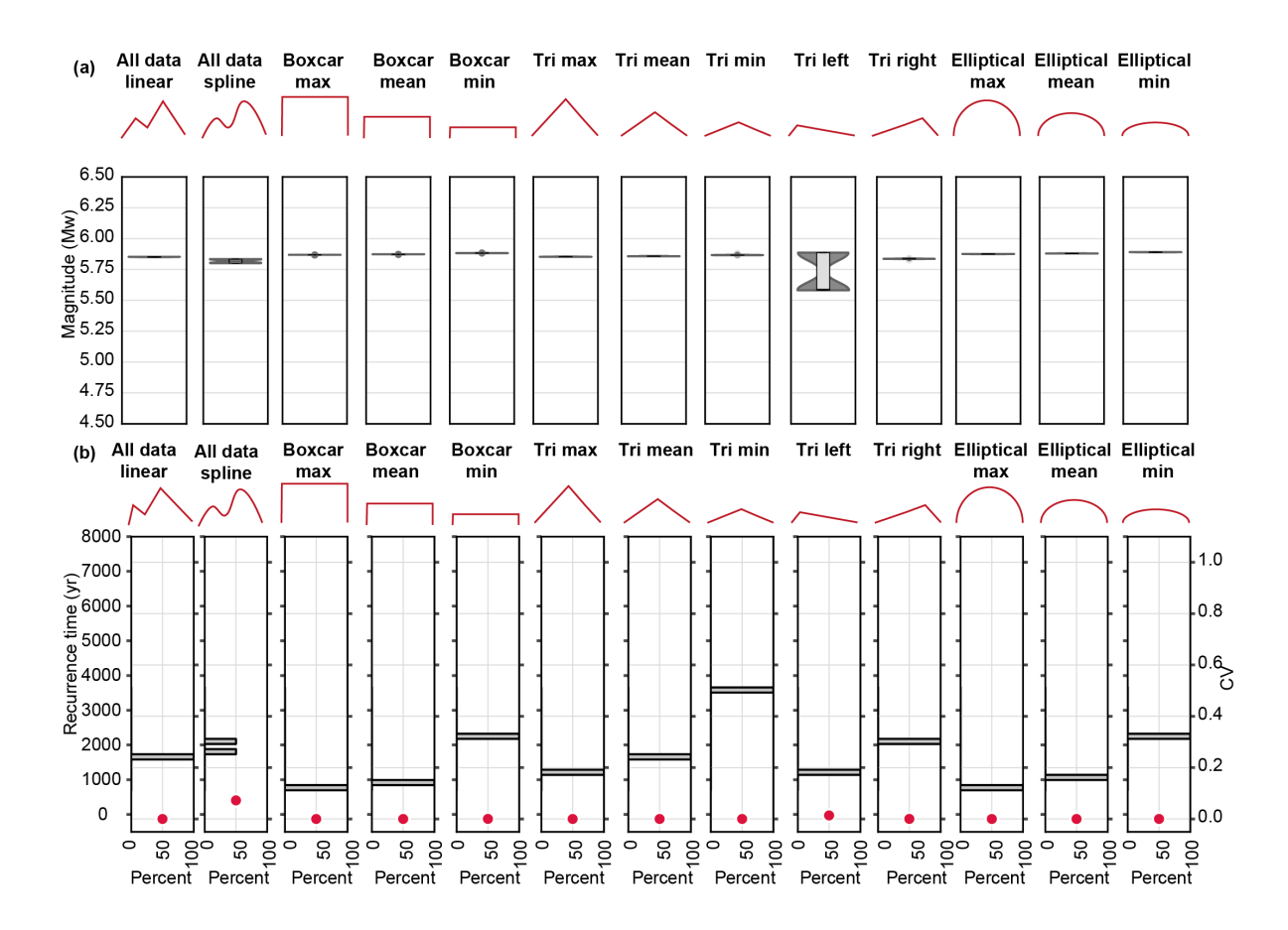


Figure S4: (a) Magnitude-frequency distribution shown as kernel-density functions for model with a=0.001 and b=0.004 (a/b=0.25); **(b)** Coefficient of variation (CV, red dots) and histogram of recurrence time (T_r, grey bars) for each simulation. For descriptions of the slip rate profiles, see Fig. 3 in the main text.

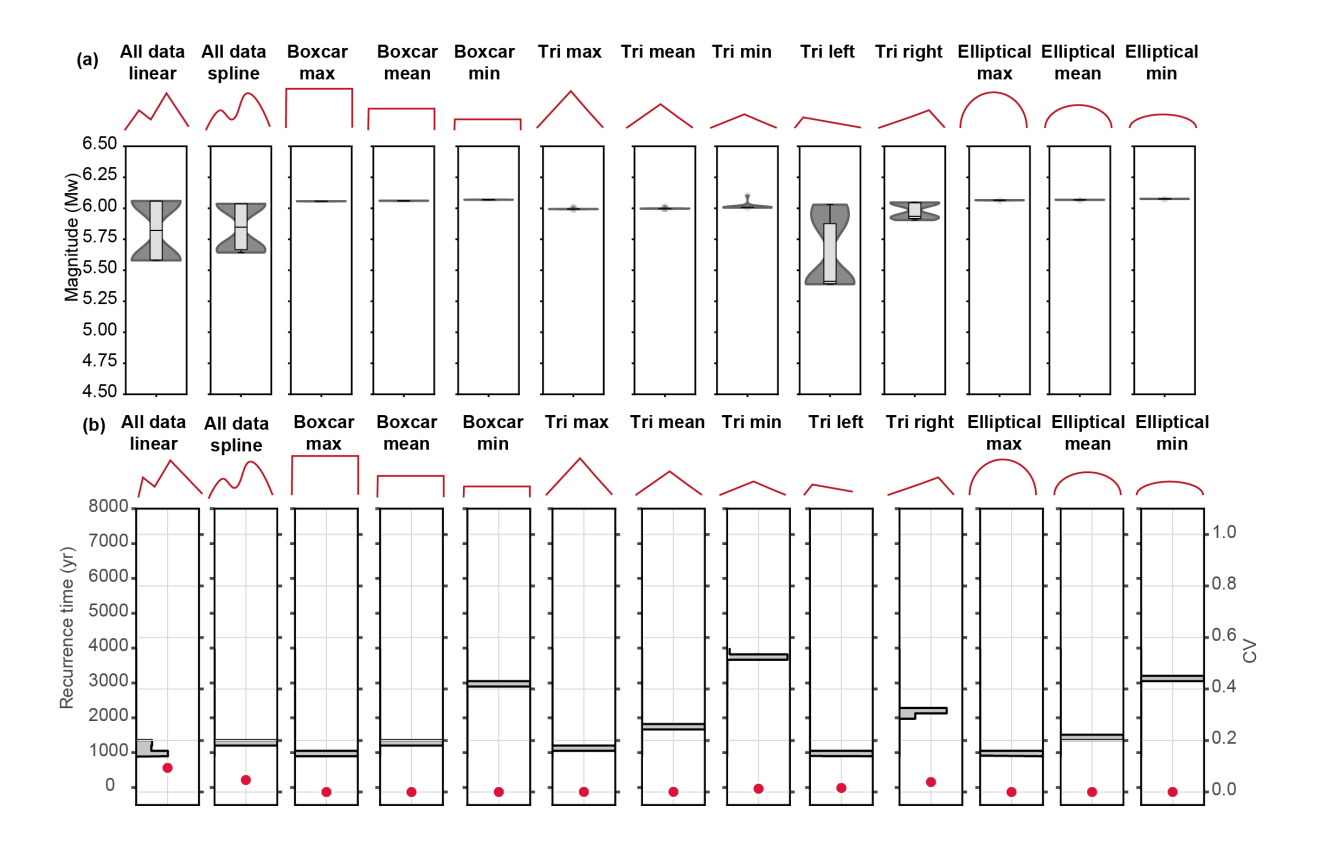


Figure S5: (a) Magnitude-frequency distribution shown as kernel-density functions for model with a=0.001 and b=0.006 (a/b=0.17); **(b)** Coefficient of variation (CV, red dots) and histogram of recurrence time (T_r, grey bars) for each simulation. For descriptions of the slip rate profiles, see Fig. 3 in the main text.

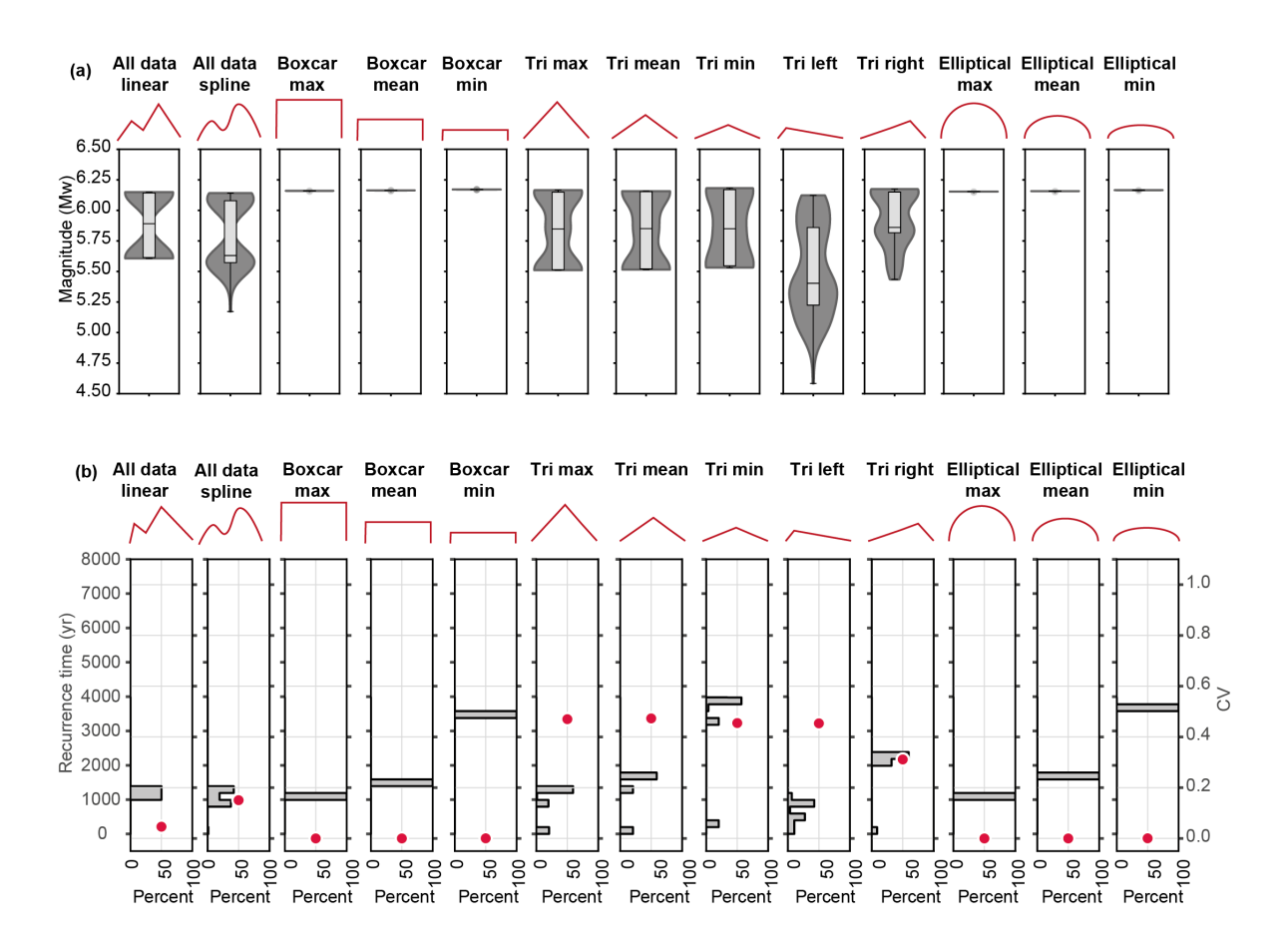


Figure S6: (a) Magnitude-frequency distribution shown as kernel-density functions for model with a=0.001 and b=0.008 (a/b=0.125); **(b)** Coefficient of variation (CV, red dots) and histogram of recurrence time (T_r, grey bars) for each simulation. For descriptions of the slip rate profiles, see Fig. 3 in the main text.

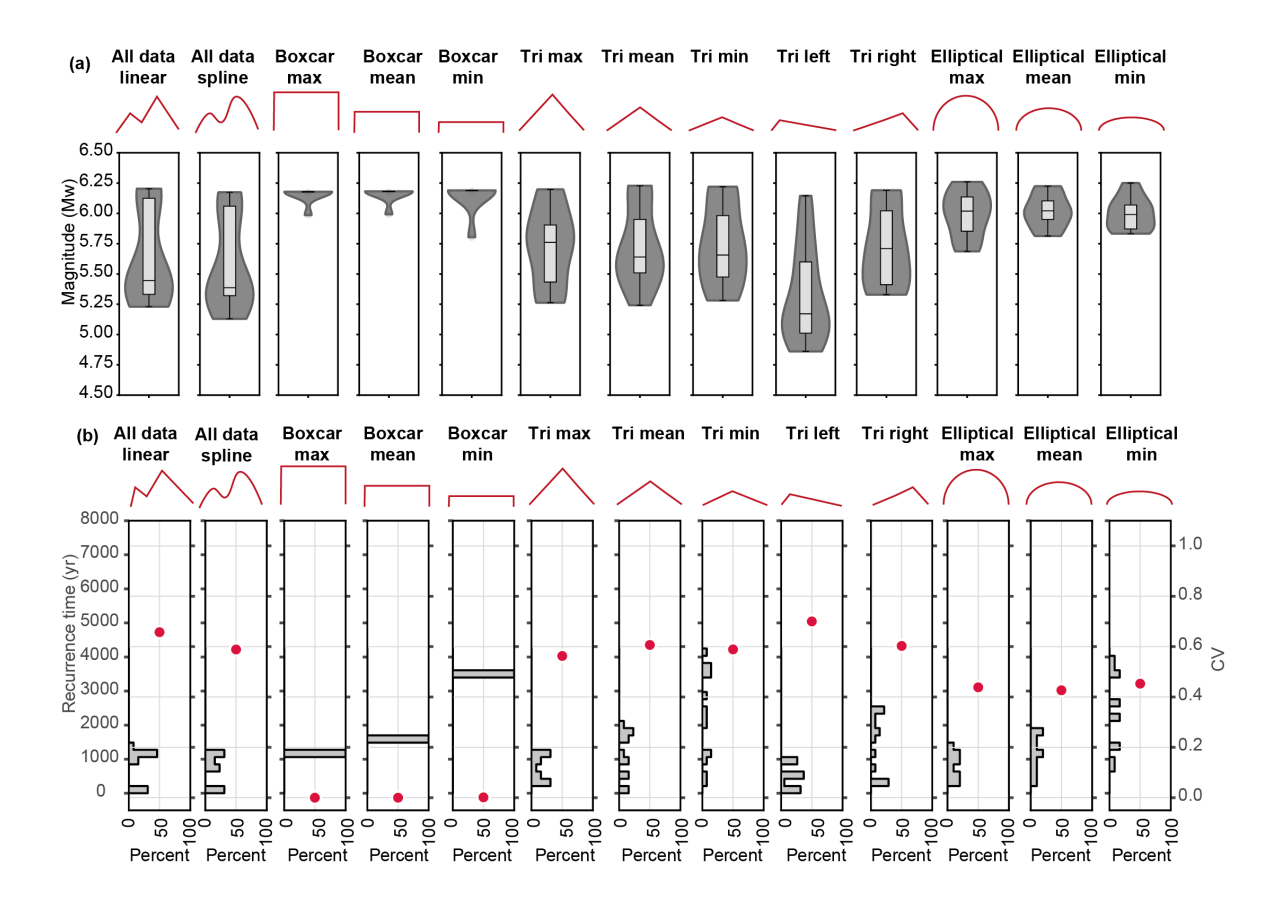


Figure S7: (a) Magnitude-frequency distribution shown as kernel-density functions for model with a=0.001 and b=0.01 (a/b=0.1); **(b)** Coefficient of variation (CV, red dots) and histogram of recurrence time (T_r, grey bars) for each simulation. For descriptions of the slip rate profiles, see Fig. 3 in the main text.

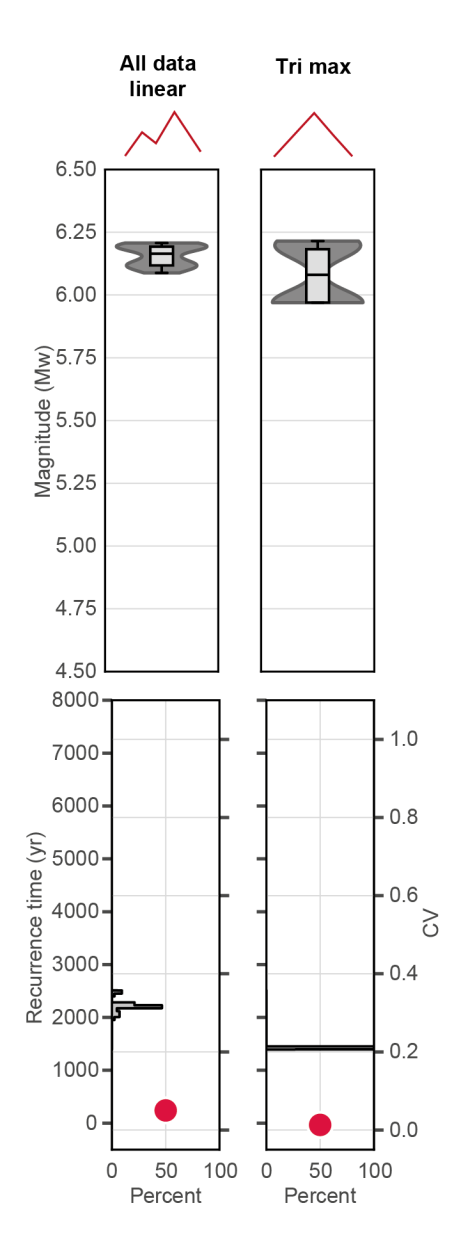


Figure S8: (a) Magnitude-frequency distribution shown as kernel-density functions for models with slip-rate maxima towards the middle of the fault and tapered values towards the bottom **(b)** Coefficient of variation (CV, red dots) and histogram of recurrence time (T_r, grey bars) for each simulation. For descriptions of the slip rate profiles, see Fig. 3 in the main text.

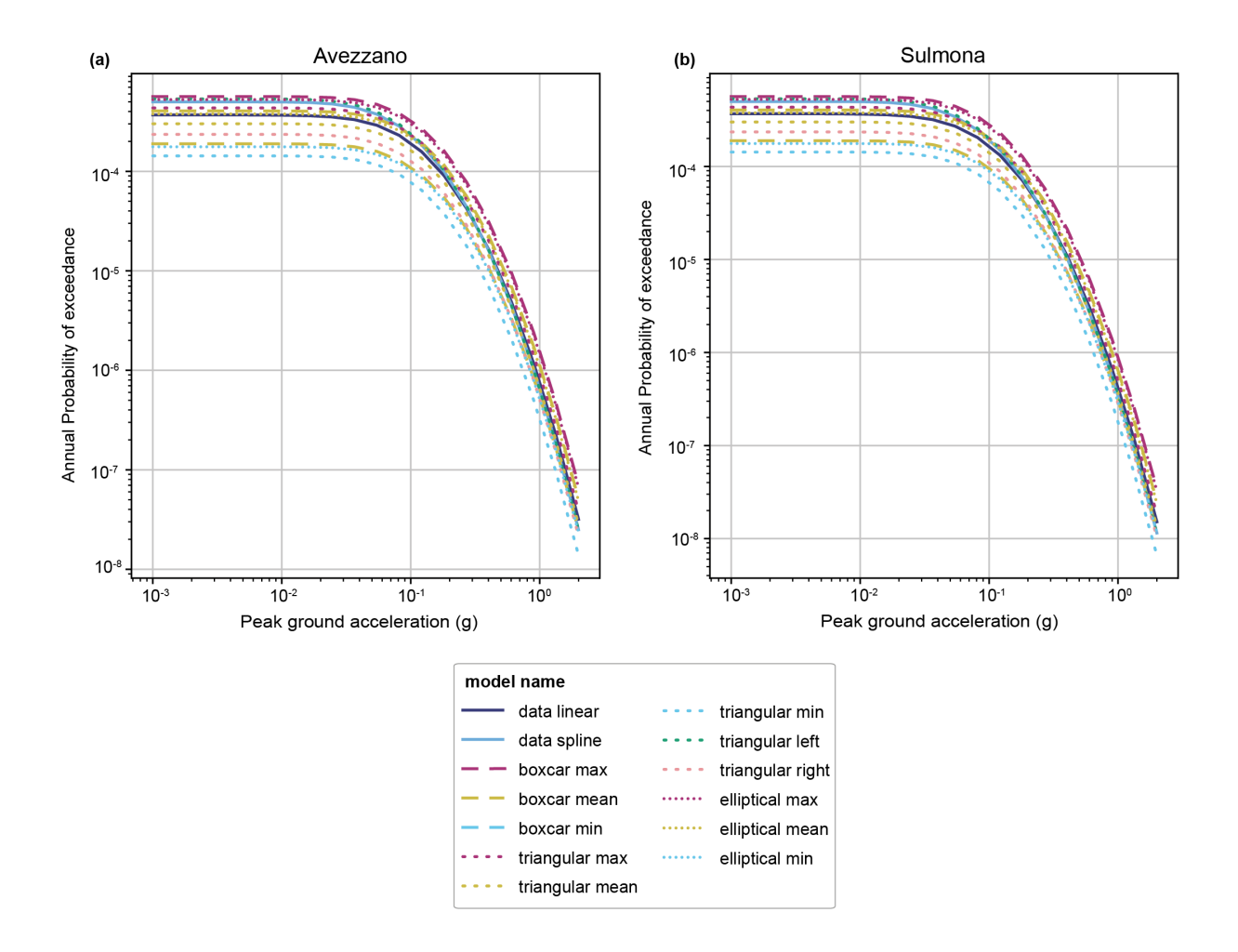


Figure S9: Hazard curves of annual probability of exceedance for a given peak ground acceleration for the Parasano-Pescina fault at the sites (a) Avezzano and (b) Sulmona (for site locations relative to the fault trace, see Fig. 1)

References

Allam, A. A., K. A. Kroll, C. W. D. Milliner, and K. B. Richards-Dinger (2019). Effects of Fault Roughness on Coseismic Slip and Earthquake Locations, *Journal of Geophysical Research: Solid Earth* **124**, no. 11, 11336–11349, doi: 10.1029/2018JB016216.

Barbot, S. (2019). Slow-slip, slow earthquakes, period-two cycles, full and partial ruptures, and deterministic chaos in a single asperity fault, *Tectonophysics* **768**, 228171, doi: 10.1016/j.tecto.2019.228171.

Cattania, C. (2019). Complex Earthquake Sequences On Simple Faults, *Geophysical Research Letters* **46**, no. 17–18, 10384–10393, doi: 10.1029/2019GL083628.

- Cattania, C., and P. Segall (2019). Crack Models of Repeating Earthquakes Predict Observed Moment-Recurrence Scaling, *Journal of Geophysical Research: Solid Earth* **124**, no. 1, 476–503, doi: 10.1029/2018JB016056.
- Cowie, P. A., R. J. Phillips, G. P. Roberts, K. McCaffrey, L. J. J. Zijerveld, L. C. Gregory, J. Faure Walker, L. N. J. Wedmore, T. J. Dunai, S. A. Binnie, *et al.* (2017). Orogen-scale uplift in the central Italian Apennines drives episodic behaviour of earthquake faults, 1, *Sci Rep* 7, no. 1, 44858, doi: 10.1038/srep44858.
- Dieterich, J. H. (1979). Modeling of rock friction 1. Experimental results and constitutive equations, Journal of Geophysical Research: Solid Earth 84, no. B5, 2161–2168, doi: 10.1029/JB084iB05p02161.
- Dieterich, J. H., and D. E. Smith (2010). Nonplanar Faults: Mechanics of Slip and Off-fault Damage, in *Mechanics, Structure and Evolution of Fault Zones* Y. Ben-Zion, and C. Sammis(Editors), Birkhäuser, Basel, 1799–1815, doi: 10.1007/978-3-0346-0138-2_12.
- Faure Walker, J. P., G. P. Roberts, P. A. Cowie, I. Papanikolaou, A. M. Michetti, P. Sammonds, M. Wilkinson, K. J. W. McCaffrey, and R. J. Phillips (2012). Relationship between topography, rates of extension and mantle dynamics in the actively-extending Italian Apennines, *Earth and Planetary Science Letters* **325–326**, 76–84, doi: 10.1016/j.epsl.2012.01.028.
- Faure Walker, J. P., G. P. Roberts, P. A. Cowie, I. D. Papanikolaou, P. R. Sammonds, A. M. Michetti, and R. J. Phillips (2009). Horizontal strain-rates and throw-rates across breached relay zones, central Italy: Implications for the preservation of throw deficits at points of normal fault linkage, *Journal of Structural Geology* **31**, no. 10, 1145–1160, doi: 10.1016/j.jsg.2009.06.011.
- Faure Walker, J. P., F. Visini, G. Roberts, C. Galasso, K. McCaffrey, and Z. Mildon (2019). Variable Fault Geometry Suggests Detailed Fault-Slip-Rate Profiles and Geometries Are Needed for Fault-Based Probabilistic Seismic Hazard Assessment (PSHA), *Bulletin of the Seismological Society of America* **109**, no. 1, 110–123, doi: 10.1785/0120180137.
- Heimisson, E. R. (2020). Crack to pulse transition and magnitude statistics during earthquake cycles on a self-similar rough fault, *Earth and Planetary Science Letters* **537**, 116202, doi: 10.1016/j.epsl.2020.116202.
- Lapusta, N., J. R. Rice, Y. Ben-Zion, and G. Zheng (2000). Elastodynamic analysis for slow tectonic loading with spontaneous rupture episodes on faults with rate- and state-dependent friction, *Journal of Geophysical Research: Solid Earth* **105**, no. B10, 23765–23789, doi: 10.1029/2000JB900250.
- Marone, C. (1998). Laboratory-Derived Friction Laws and Their Application to Seismic Faulting, *Annual Review of Earth and Planetary Sciences* **26**, no. 1, 643–696, doi: 10.1146/annurev.earth.26.1.643.
- Papanikolaou, I. D., G. P. Roberts, and A. M. Michetti (2005). Fault scarps and deformation rates in Lazio–Abruzzo, Central Italy: Comparison between geological fault slip-rate and GPS data, *Tectonophysics* **408**, no. 1, 147–176, doi: 10.1016/j.tecto.2005.05.043.
- Roberts, G. P., and A. M. Michetti (2004). Spatial and temporal variations in growth rates along active normal fault systems: an example from The Lazio–Abruzzo Apennines, central Italy, *Journal of Structural Geology* **26**, no. 2, 339–376, doi: 10.1016/S0191-8141(03)00103-2.
- Rodriguez Piceda, C. (2025). 3D seismic cycle model with variable slip-rate and hazard calculations, Zenodo, doi: 10.5281/zenodo.15101946.
- Rubin, A. M., and J.-P. Ampuero (2005). Earthquake nucleation on (aging) rate and state faults, *Journal of Geophysical Research: Solid Earth* **110**, no. B11, doi: 10.1029/2005JB003686.

Ruina, A. (1983). Slip instability and state variable friction laws., *Journal of Geophysical Research* **88**, no. B12, 10359–10370, doi: 10.1029/JB088iB12p10359.